



Strain-induced phase transition from antiferromagnet to altermagnetAtasi Chakraborty ^{1,*}, Rafael González Hernández,² Libor Šmejkal,^{1,3} and Jairo Sinova ^{1,4}¹*Institut für Physik, Johannes Gutenberg Universität Mainz, D-55099 Mainz, Germany*²*Departamento de Física y Geociencias, Universidad del Norte, Barranquilla 080020, Colombia*³*Institute of Physics, Academy of Sciences of the Czech Republic, Cukrovarnická 10, 162 00 Praha 6, Czech Republic*⁴*Department of Physics, Texas A&M University, College Station, Texas 77843-4242, USA*

(Received 20 February 2024; revised 2 April 2024; accepted 12 April 2024; published 24 April 2024)

The newly discovered altermagnets are unconventional collinear compensated magnetic systems, exhibiting even (d , g , or i wave) spin-polarization order in the band structure, setting them apart from conventional collinear ferromagnets and antiferromagnets. Altermagnets offer advantages of spin-polarized current akin to ferromagnets, and THz functionalities similar to antiferromagnets, while introducing new effects like spin-splitter currents. A key challenge for future applications and functionalization of altermagnets is to demonstrate controlled transitioning to the altermagnetic phase from other conventional phases in a single material. Here we prove a viable path toward overcoming this challenge through a strain-induced transition from an antiferromagnetic to an altermagnetic phase in ReO_2 . Combining spin group symmetry analysis and *ab initio* calculations, we demonstrate that under compressive strain ReO_2 undergoes such transition, lifting the Kramers degeneracy of the band structure of the antiferromagnetic phase in the nonrelativistic regime. In addition, we show that this magnetic transition is accompanied by a metal-insulator transition, and calculate the distinct spin-polarized spectral functions of the two phases, which can be detected in angle-resolved photoemission spectroscopy experiments.

DOI: [10.1103/PhysRevB.109.144421](https://doi.org/10.1103/PhysRevB.109.144421)**I. INTRODUCTION**

The recently discovered altermagnets (AMs) are a new, third class of collinear compensated magnetic materials [1–9] that go beyond the conventional collinear ferromagnetic and antiferromagnetic classes. AMs are compensated magnetic ordered systems exhibiting unconventional spin-polarized d , g , or i wave order in the nonrelativistic band structure, originating from local sublattice symmetries in direct space. This gives rise to properties unique to altermagnets (e.g., the spin-splitter effect), while also giving similar properties of ferromagnets (FMs) (e.g., polarized currents) and antiferromagnets (AFMs) (e.g., THz spin dynamics and zero net magnetization). The unconventional time reversal symmetry (TRS) breaking in momentum space in AMs arises from the spin point-group symmetries [2,10] that interchange sublattices with opposite spins only via a rotation (proper or improper).

The merged advantageous technological characteristics of AMs make controlling the transition between AMs and FMs/AFMs not only of fundamental interest, but also serves as a foundational element for device applications. Tunable AMs can be used in data storage, sensors, and spintronics applications by exploiting, e.g., efficient spin current generation [11–13], giant magnetoresistance [6], spin-splitter torques [14,15], anomalous Hall effects [1,16–18], and Josephson effects [19]. Because of the intricate connection of crystal

symmetry and altermagnetism, mechanical deformation offers the most direct route to modify electronic properties solely by altering crystal symmetries, without necessitating additional electronic perturbations or chemical modifications. Tensile strain and hydrostatic pressure are established reliable techniques to directly control lattice parameters and crystal symmetry, and hence can control phases connected with magnetism, superconductivity, and topology [20–24].

In this article, we propose to use strain as a controlling parameter to tune magnetic transition from a conventional AFM to an AM. We choose ReO_2 as a working platform to explore phase transitions with mechanical deformations, because of its nontrivial topology emerging from nonsymmorphic symmetries [25,26] and its recently observed structural phases [27–29]. Bulk ReO_2 primarily crystallizes in monoclinic α and orthorhombic β phases. The topological characteristics of orthorhombic β - ReO_2 are of particular interest due to its hourglass-like Dirac chains [25] and proposed to order antiferromagnetically around ~ 4.2 K, while the monoclinic phase of ReO_2 is less explored. However, a recent experimental report has revealed a transformation from the monoclinic phase into the tetragonal rutile (R) phase driven by compressive lattice strain with decreasing film thickness [27]. The spin group theory utilized to classify and characterize altermagnets [2] predicts R - ReO_2 to be a d -wave AM candidate. Although there are no reports on magnetic transitions in the magnetic system class of ReO_2 , the hydrostatic-pressure-induced continuous “martensitic” transition between the monoclinic to the tetragonal phase in the context of other transitions, e.g., the metal-insulator transition (MIT), for the ZrO_2 systems, to

*Corresponding author: atasi.chakraborty@uni-mainz.de

which ReO_2 belongs, has been well studied in the literature [30–32].

Using both symmetry analysis and state-of-the-art density functional theory (DFT) calculations, we show that the pressure-induced deformation and the corresponding changes in the crystal symmetry lead to an AFM to AM crossover in ReO_2 . Further, we investigate the strain-induced change in topology and nodal crossing within the same chemical composition of ReO_2 . As the AFM to AM transition is insensitive to susceptibility measurements, we provide a way to experimentally sense the phase transition through spin-polarized angle-resolved photoemission spectroscopy (S-ARPES) experiments [33,34].

II. COMPUTATIONAL METHODS

To perform the *ab initio* calculations, we used density functional theory (DFT) in the plane wave basis set. We used the Perdew-Burke-Ernzerhof (PBE) [35] implementation of the generalized gradient approximation (GGA) for the exchange correlation. This was combined with the projector augmented wave potentials [36,37] as implemented in the Vienna *ab initio* simulation package (VASP) [38,39]. GGA calculations are carried out with and without Coulomb correlation (Hubbard U) and spin-orbit coupling (SOC). The calculations were done with the usual value of U and Hund’s coupling J_H chosen for Re with $U_{\text{eff}} (\equiv U - J_H) = 1.5$ eV in the Dudarev scheme [40]. The SOC is included in the calculations as a second variational form to the original Hamiltonian. The kinetic energy cutoff of the plane wave basis for the DFT calculations was chosen to be 520 eV. The Γ -centered $9 \times 9 \times 17$ and $10 \times 10 \times 10$ k -point grids are used to perform the momentum-space calculations for the Brillouin zone (BZ) integration of tetragonal and monoclinic phases, respectively. To calculate the surface spectral function for finite geometry slabs of R - and α - ReO_2 , we construct the tight-binding model Hamiltonian by using atom-centered Wannier functions within the VASP2WANNIER90 [41] codes. Utilizing the obtained tight-binding model, we calculate the surface spectral function using the iterative Green’s function method, as implemented in the WannierTools package [42].

III. RESULTS

A. Strain-mediated phase transition

In this section, we provide the structural comparison between the usual monoclinic (α -) phase and the nontrivial tetragonal (R -) phase of ReO_2 , and explore the structural transition. Bulk α - ReO_2 crystallizes in monoclinic space group $P2_1/c$ (No. 14). The distorted ReO_6 octahedra accommodating the nearest neighbor Re-O bonds (~ 1.86 – 2.13 Å) form a geometrical network which is edge sharing in one direction and corner shared along the other. A recent experimental study validates the presence of tetragonal R - ReO_2 induced by strain, which exhibits the space group $P4_2/mnm$ [27]. Here, we will calculate the transition pathways between the two phases. We summarize the local structural parameters for both R - and α - ReO_2 in Table I. Our calculations show that the α - to R -phase transition is accompanied by a $\sim 2.5\%$ volume collapse per formula unit. The unit cell (u.c.) structure along with

TABLE I. Comparison of the tetragonal and monoclinic lattice parameters. In the monoclinic unit cell each ReO_6 octahedra contains six different bond lengths of octahedra. Minimum and maximum Re-O bond lengths are noted with symbol.††

	Tetragonal	Monoclinic
β	90°	119.55°
Re-O (Å)	1.96, 2.04	1.86 – $2.13^{\dagger\dagger}$
Re-Re [edge] (Å)	2.68	3.07
Re-Re [corner] (Å)	3.75	3.55, 3.61, 3.81

the schematic of the “martensitic” kind transition is shown in the top panel of Fig. 1. The unit cells of α - and R - ReO_2 are plotted in Figs. 1(a) and 1(b), respectively.

In order to investigate the impact of pressure and to track the phase transition, we have carried out numerical calculations within DFT for different structures modulating the unit cell volume for both phases. We have employed the Murnaghan equation of state [43,44] to fit the obtained total energy from self-consistent DFT calculations:

$$E(V) = E_0 + \frac{B_0 V}{B'_0} \left[\frac{(V_0/V)^{B'_0}}{B'_0 - 1} + 1 \right] - \frac{B_0 V_0}{B'_0 - 1}. \quad (1)$$

Here V_0 is the equilibrium volume and $B_0 = -V(\partial P/\partial V)$ is the bulk modulus evaluated at V_0 . The typical values of B'_0 (pressure derivative of B_0), used as a measure of stiffness of

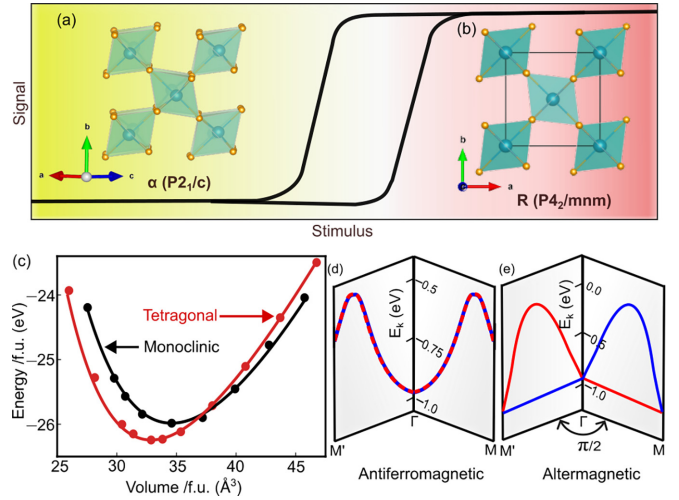


FIG. 1. Phase transition. The top panel depicts a schematic representation of the martensitic structural transition from a monoclinic phase to a tetragonal phase under the influence of external stimuli, e.g., strain, temperature. The change in spin-polarized current induced voltage or resistivity can be used as an experimental signal to probe the phase transition. Insets (a) and (b) show the unit cells of monoclinic α - ReO_2 and tetragonal R - ReO_2 , respectively. (c) Birch Murnaghan fitting of DFT cohesive energy vs volume of the two ReO_2 phases. The presence of a stable tetragonal phase under compressive strain is in agreement with experimental observations. Spin-polarized energy dispersions of antiferromagnetic monoclinic (d) and altermagnetic tetragonal (e) ReO_2 along orthogonal momentum paths.

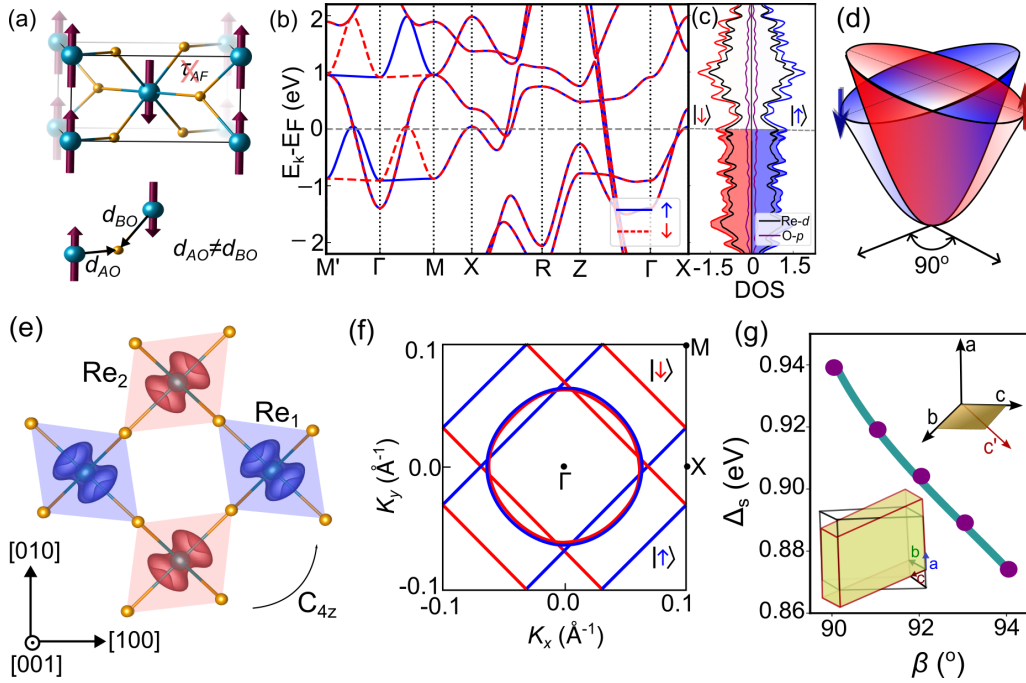


FIG. 2. Nonrelativistic spin splitting. (a) The crystal structure and bond connectivity of $R\text{-ReO}_2$ in ground state magnetic configuration. The inset shows the different Re-O bond lengths due to distribution of ligands over noncentrosymmetric sites. (b) and (c) represent the spin-resolved band and density of states plot of $R\text{-ReO}_2$ in the absence of SOC. The energy axis is scaled with respect to Fermi energy, E_F . The presence of a fully compensated density of states indicates zero magnetization, while the existence of momentum-dependent splitting in band dispersion indicates the broken TRS. (d) Schematics of momentum-resolved spin splitting for d -wave AM candidate $R\text{-ReO}_2$. (e) Magnetization density plot of neighboring Re sublattices is orthogonal and preserves the fourfold C_{4z} rotational symmetry. (f) Constant energy contour for $E = E_F - 0.15$ eV. This shows that the nature of the spin splitting is opposite for orthogonal momentum points. (g) Change of spin splitting (Δ_s) with deviation of crystallographic angle β from 90° . The insets show the nature of deformation of the crystal unit cell with β variation.

the material, are between 4 and 7 [45]. We have included the variation of cohesive energy with volume in Fig. 1(c) for both α - and $R\text{-ReO}_2$. It clearly shows that below a critical pressure, the compressive strain provides a way to stabilize the tetragonal structure with respect to the usual monoclinic phase, in full agreement with the experimental observation [27]. In the rest of the article we establish that this is not merely a structural transition; rather it completely changes the nature of the magnetism promoting an AFM [see Fig. 1(d)] to AM [see Fig. 1(e)] ground state in the same chemical composition of ReO_2 . In the following we discuss the contrasting electronic, magnetic, and topological properties for both R - and $\alpha\text{-ReO}_2$.

B. Altermagnetic tetragonal $R\text{-ReO}_2$

1. Nonrelativistic magnetic order and symmetry analysis

Having established the structural transition mechanism to the high-pressure tetragonal phase, we now explore the electronic structure of the altermagnetic phase and characterize this from a microscopic and structural origin. The two Re sublattices of $R\text{-ReO}_2$, contained within the trigonally distorted octahedral environment, order with opposite spin moments, i.e., compensated magnetization [see Fig. 2(a)]. To analyze the effect of crystal symmetry and the exchange-driven altermagnetic ordering, we set initially the SOC to zero. Our DFT calculations within the GGA+ U scheme indicate that the state with antiparallel arrangement of spins is substantially lower in

energy of value 92.9 meV/Re (111.8 meV/Re) than its ferromagnetic (nonmagnetic) counterpart. Our result agrees well with the previous first-principles study on $R\text{-ReO}_2$ [28]. The coexistence of metallic and AM behavior in $R\text{-ReO}_2$ is robust against variation of the Coulomb correlation (see Appendix B for details). Although no experimental studies of tetragonal $R\text{-ReO}_2$ for magnetism have been reported, the presence of an AFM ground state has been proposed around ~ 4.2 K for its orthorhombic β phase [25]. Notably, the presence of antiparallel spin ordering within the tetragonal stoichiometry has been studied and confirmed in the sister compounds, e.g., RuO_2 [16] and CoF_2 [46].

In Fig. 2(b) we plot the nonrelativistic spin-polarized band structures along different high-symmetry k points for collinear compensated spin order. The total magnetization of the unit cell vanishes as can be seen in the density of states plot of Fig. 2(c). The distribution of ligand O atoms over the noncentrosymmetric $4f$ Wyckoff positions promotes unequal bond lengths with two different Re sublattices and gives rise to the altermagnetic spin symmetry which interchanges sublattices with opposite spins via a rotation, and leads in turn to broken TRS in the electric band structure. We find momentum-dependent splitting between up and down spins along the ΓM path. The sign of the spin splitting is opposite for two orthogonal paths as can be seen between ΓM and $\Gamma M'$ directions in Fig. 2(a). The schematic of the spin splitting is plotted in Fig. 2(d) in agreement with its d -wave AM

phase. The details of d -wave AM from the spin group theory perspective are included in Appendix A for completeness [2]. We have plotted the spin densities of the two Re-sublattices in Fig. 2(e). The anisotropic magnetization densities of the two sublattices are connected through fourfold crystal rotation. The constant energy contour near the Fermi energy, at $E_k - E_F = -0.15$ eV, shows that $\epsilon(\mathbf{k}_\uparrow) \neq \epsilon(-\mathbf{k}_\downarrow)$, confirming the breakdown of the TRS. Next we analyze our *ab initio* results from the crystal symmetry viewpoint.

In the absence of SOC, the real space and the spin spaces are decoupled. The resulting nonrelativistic space group has the following spin symmetry,

$$[E||mmm] + [C_2||G\backslash mmm|\mathbf{t}'], \quad (2)$$

where mmm and $G\backslash mmm$ include respectively $\{E, P, C_{2z}, C_{2d}, C_{2d\perp}, \mathcal{M}_z, \mathcal{M}_d, \mathcal{M}_{d\perp}\}$ and $\{C_{2y}, C_{2x}, \pm C_{4z}^\pm, \mathcal{M}_x, \mathcal{M}_y\}$. The \hat{d} and \hat{d}_\perp axes are along $\hat{x} + \hat{y}$ and $\hat{x} - \hat{y}$, respectively. Here the operation of the left (right) of the parentheses acts solely on the spin (real) space. The detailed description of the symmetry operations is included in Appendix A. Here \mathbf{t}' is the half translation along the body diagonal. If the opposite spin sublattices are not connected by a translation or inversion, the Kramers degeneracy of the spin up and down channels gets lifted, promoting an alternating Zeeman-like band splitting even in the absence of SOC, and connecting opposite spin states whose momentum is related by the C_{4z} rotation. We refer to these opposite spin bands as an altermagnetic pair throughout the rest of the article. The two sublattices containing opposite spins are related by the screw rotation $\{C_{4z}|\mathbf{t}'\}$ in R - ReO_2 , as can be seen in the relative octahedral orientation and spin density plot of Fig. 2(e). As a result, we see a spin splitting between altermagnetic-pair bands along the ΓM paths within the nonrelativistic limit. As demonstrated in Eq. (2), the $[C_2||\mathcal{M}_{x(y)}]$ yields $\epsilon(k_x, k_y, k_z, \sigma) = \epsilon(\mp k_x, \pm k_y, k_z, -\sigma)$. Thus, the opposite-spin altermagnetic-pair bands are degenerate for both $k_x = 0, \pi$ and $k_y = 0, \pi$ planes within the nonrelativistic limit as shown in Fig. 9 of Appendix D.

Next we discuss the impact a small structural deformation has on the nonrelativistic energetics. The crystal symmetry analysis suggests that the primary difference between the monoclinic unit cell and its tetragonal unit cell is the deviation of the crystallographic angle β from 90° ; i.e., the crystal axis c is no longer perpendicular to the a - b plane, as shown in the inset of Fig. 2(g). To induce this typical distortion we have constructed hypothetical structures from the R - ReO_2 unit cell by manually increasing the angle β slightly from 90° . For energy minimization, we have done ionic relaxation of each structure using the conjugate-gradient algorithm until the Hellman-Feynman forces on each atom are less than the tolerance value of 0.01 eV/Å. In Fig. 2(g) we show the change in spin splitting with angle β . The reduction in spin splitting with increase in β drives the system toward an AFM state. However, there exist other effects in realistic situations, such as various magnetic arrangements, atomic reconstructions, differences between magnetic and crystal unit cells (i.e., propagation vector $\mathbf{Q} \neq 0$), etc. Hence the details of electronic structure in the monoclinic phase are discussed later in Sec. III C.

2. Effect of spin-orbit coupling and magnetic anisotropy

The presence of heavy $4d/5d$ transition metal elements within any system can influence the strength of the SOC, ultimately determining the ground state characteristics of the magnetic order [47–51]. In the following we investigate how the crystal symmetry analysis of the spin splitting proceeds in the relativistic regime. We next incorporate SOC in our calculations, leading to magnetic anisotropy that leads to a preferred axis quantization. This leads to different magnetic space groups for the different quantization axis, relevant for analyzing the topological properties of their respective states.

In Fig. 3, panels (a), (b), and (c), we plot the relativistic band dispersion with spin along the [001], [100], and [110] axes, respectively. The corresponding magnetic space groups are marked in the respective plots. As the magnetic Re atoms occupy the Wyckoff site $2a$ in the unit cell, the ground state magnetic space group only allows collinear magnetic arrangements (see allowed moment per Wyckoff positions for ground state configuration in the table in Fig. 9 of Appendix D) even in the presence of SOC. We find that changing the spin quantization from the out-of-plane to in-plane direction now opens up the degeneracy of the opposite spin bands at the Γ point; i.e., a small net magnetization is present, proportional to the SOC. Our *ab initio* calculations predict a [001] spin quantization axis with magnetocrystalline anisotropy (MCA) energy ~ 3 meV. The polar plot of the MCA energy is shown in Fig. 3(d) when the spin directions are rotated on the xz (green) and xy (red) planes, respectively. This low anisotropy energy makes R - ReO_2 a promising material for adjusting the Néel vector for anomalous transport experiments. Our calculation suggests that finite electron doping can promote in-plane magnetocrystalline anisotropy in R - ReO_2 (see Appendix C for detailed discussion). The ground state characteristics of R - ReO_2 closely resemble those of the significant d -wave AM RuO_2 .

3. Relativistic splitting and nodal crossings

In this section we will discuss how inclusion of SOC additionally splits the altermagnetic pair in certain high-symmetry directions and changes the nodal structures. Hence the nodal planes/lines/points present in the nonrelativistic regime are no longer preserved or break into parts depending on the spin quantization. First we analyze the possibility of a nodal plane for the ground state magnetic configuration, with quantization axis [001] and magnetic space group $P4_2/mnm'$, containing the following symmetry operations:

$$\{E, P, C_{2z}, \mathcal{M}_z\} + \mathbf{t}'\{C_{2x}, C_{2y}, \mathcal{M}_x, \mathcal{M}_y\} \\ + \mathcal{T}\{C_{2d}, C_{2d\perp}, \mathcal{M}_d, \mathcal{M}_{d\perp}\} + \mathbf{t}'\mathcal{T}\{\pm C_{4z}^\pm\}.$$

Here \mathcal{T} is the time-reversal operation. The \mathcal{M}_d and $\mathcal{M}_{d\perp}$ mirror planes, containing the opposite sublattices, can host the nodal crossings. The nonrelativistic nodal crossings, which are preserved in the presence of SOC, are therefore those that intersect with these \mathcal{M}_d and $\mathcal{M}_{d\perp}$ mirror planes, i.e., ΓZ , AM , and AM' lines. These sharp nodal lines in the presence of SOC can be seen in Fig. 3(e).

Next we explore the possibility of any other nodal planes within the ground state R - ReO_2 . The operation $\mathbf{t}'\mathcal{T}\{\pm C_{4z}^\pm\} =$

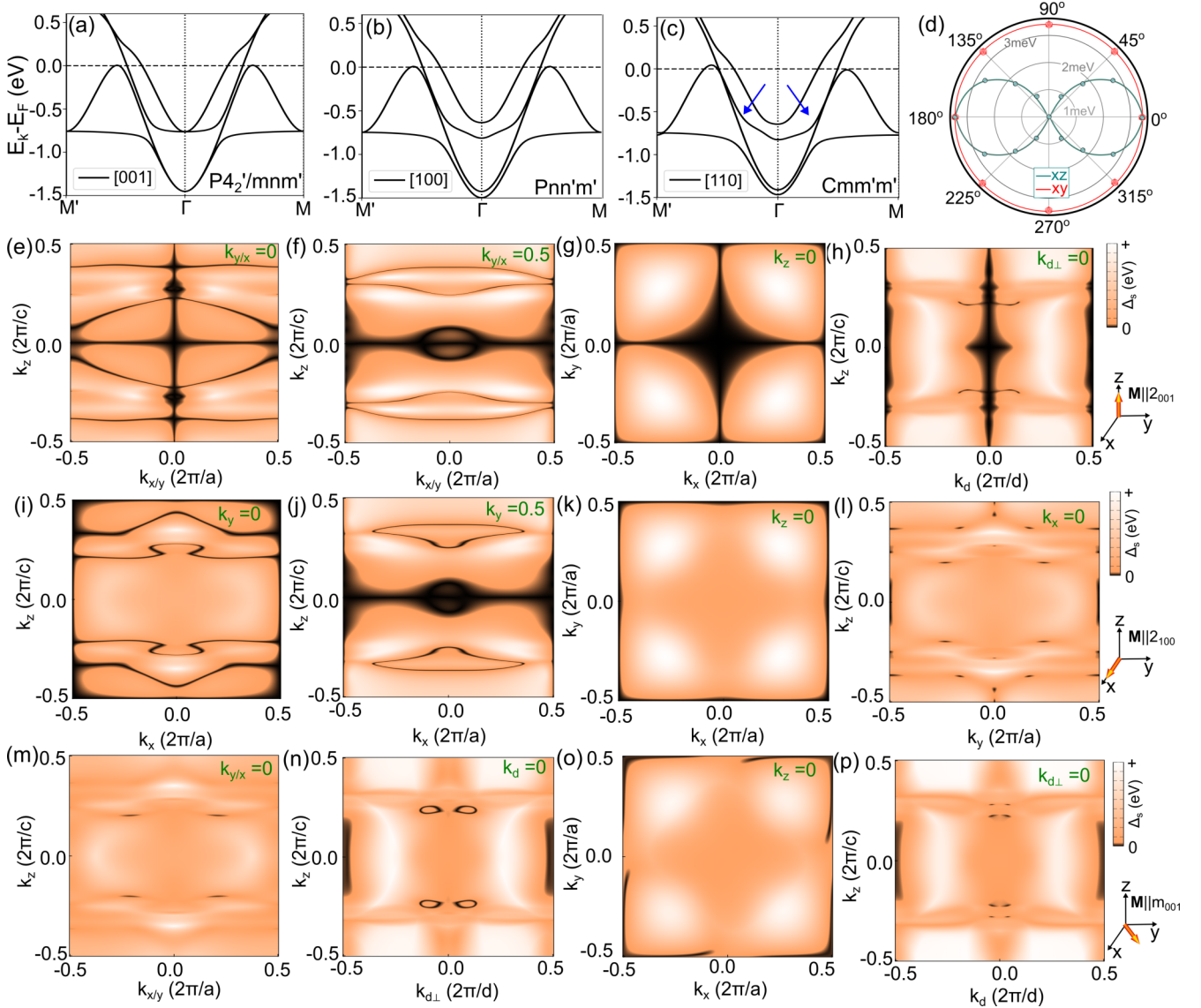


FIG. 3. Spin-orbit coupling and Nodal crossing. The band dispersion along two orthogonal spin-split ΓM high-symmetry directions for out-of-plane [001] (a) and in-plane spin quantization [100] (b) and [110] (c). The SOC induces asymmetry in the bulk band dispersion for magnetic anisotropy along [110]. (d) Calculated magnetic anisotropy energy per unit cell when spin direction is rotated in the xz (green) and xy (red) planes in the AM configuration for $U_{\text{eff}} = 1.5$ eV. The Re spins prefer easy-axis magnetic anisotropy along z axis. The nodal crossings between the first valence AP for different planes are plotted for spin quantization along [001] (e)–(h), [100] (i)–(l), and [110] (m)–(p), respectively. Here $\hat{d} = \hat{x} + \hat{y}$ and $\hat{d}_{\perp} = \hat{x} - \hat{y}$. The nodal crossings and Weyl points drastically change for change in spin quantization. Due to the band asymmetry in (c), there exists nodal loop in (n) but no such nodal structures in (p).

$\mathcal{T}S_{4z}^{\pm} \equiv \mathcal{A}$, where the combined effect of space operation and time reversal maps the spins of the two sublattices. The Hamiltonian is invariant under the symmetry operation \mathcal{A} , i.e., $\mathcal{A}^{-1}\mathcal{H}\mathcal{A} = \mathcal{H}$. Below we analyze the symmetry protection of the nodal planes in the presence of SOC. We consider two block wave functions $\psi_{\mathbf{k}}$ and $\psi'_{\mathbf{k}}$ which are related by this nonsymmorphic operation as $\psi'_{\mathbf{k}'} = \mathcal{T}S_{4z}\psi_{\mathbf{k}}$. The eigenvalue equation for momentum \mathbf{k}' , where $\mathbf{k}' = \mathcal{A}\mathbf{k} \neq \mathbf{k}$, is

$$E_{\mathbf{k}'}\psi'_{\mathbf{k}'} = \mathcal{H}\psi'_{\mathbf{k}'} = \mathcal{H}[\mathcal{A}\psi_{\mathbf{k}}], \quad (3)$$

$$\mathcal{A}[\mathcal{H}\psi_{\mathbf{k}}] = E_{\mathbf{k}}[\mathcal{A}\psi_{\mathbf{k}}]. \quad (4)$$

As the Hamiltonian is invariant under the symmetry operation connecting the two eigenfunctions, these must share common

eigenvalues. Now to check the orthogonality condition we calculate the overlap function,

$$\langle \psi_{\mathbf{k}} | \psi'_{\mathbf{k}'} \rangle = \langle \mathcal{A}\psi'_{\mathbf{k}'} | \mathcal{A}\psi_{\mathbf{k}} \rangle = \mathcal{A}^2 \langle \psi'_{\mathbf{k}'} | \psi_{\mathbf{k}} \rangle. \quad (5)$$

To satisfy the orthogonality condition, the left-hand side and right-hand side of Eq. (5) must be opposite in sign. By definition of the space operation, $\mathcal{A}^2 = e^{i(k_y - k_x + k_z)/2} e^{i(k_x + k_y + k_z)/2} = e^{i(k_y + k_z)}$. The two wave functions are orthogonal only if the wave vector satisfies $k_y + k_z = \pi$. But, nonrelativistic nodal planes exist only for planes $k_x = 0, \pm\pi$ and $k_y = 0, \pm\pi$ (see Fig. 9 in Appendix D), which does not satisfy the criteria of Eq. (5). Therefore for the ground state $P4_2'/mnm'$, we do not have any nodal planes. Instead we find nodal lines and Weyl points as depicted in Fig. 3.

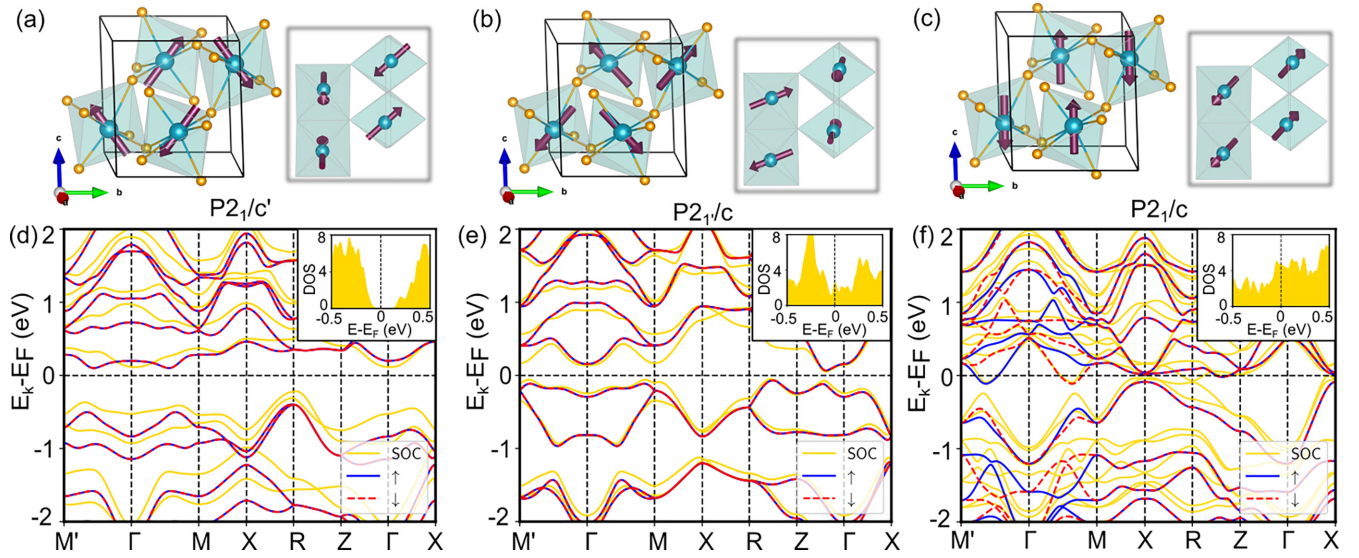


FIG. 4. Monoclinic magnetic states. Three possible antiparallel arrangements of spin of monoclinic α in (a), (b), and (c), respectively. Spin-polarized band dispersion both without (blue solid and red dashed lines) and with SOC (yellow solid line) is plotted in (d), (e), and (f) for spin configurations shown in (a), (b), and (c), respectively. Insets of (d) and (e) show corresponding density of states for each magnetic configuration of (a)–(c). The magnetic configuration plotted in (a) is the lowest energy state of α - ReO_2 .

The band crossings between altermagnetic pairs lead to several nodal lines and Weyl points. Different crystallographic planes containing the nodal crossings between the lowest valence altermagnetic pair for spin quantization along $[001]$ are plotted in Figs. 3(e)–3(h). Due to the equivalence of k_x and k_y axes relative to spin quantization direction, swapping between k_x and k_y in momentum space leads to an identical nodal structure, as shown in Figs. 3(e) and 3(f). Further, in Figs. 3(i)–3(l) and 3(m)–3(p), the nodal crossings are plotted for magnetic space groups $Pnn'm$ and $Cmm'm'$, where we have spin anisotropy along $[100]$ for the former and in-plane $[110]$ spin quantization for the latter, respectively. The nodal lines on the mirror planes will be robust against infinitesimal field perpendicular to the mirror planes. The nodal lines of altermagnetic-pair bands will be protected when the opposite spin directions are parallel (perpendicular) to the mirror plane \mathcal{M} ($\mathcal{M}' \equiv \mathcal{T}\mathcal{M}$). The SOC induces a band asymmetry along orthogonal ΓM directions, as can be seen in Fig. 3(c). As a result we get nodal loops in the $\mathbf{k}_{110} \equiv \mathbf{k}_d$ plane whereas the orthogonal plane $\mathbf{k}_{1\bar{1}0} \equiv \mathbf{k}_{d\perp}$ does not contain that. Hence, the SOC not only settles the magnetic anisotropy energy for feasibility in anomalous transport applications but also dictates the nature of nontrivial nodal lines.

C. Magnetic ground state of monoclinic α - ReO_2

In this section we will discuss the nature of magnetism for the monoclinic phase. The different arrangement of Re magnetic moments over four possible $1a$ Wyckoff sites can lead to reduction in crystal symmetries and consequently affect the electronic structure and topology of the system. The nearest neighbor ReO_6 octahedra form an edge-shared linear network in the $[\bar{1}, 1, \bar{1}]$ direction. The two nearest edge-shared octahedral chains are connected by corner sharing. The allowed antiparallel arrangements of moments at $q = 0$ can be

twofold: (A) antiferromagnetic ordering along edge-shared and a combination of antiferromagnetic and ferromagnetic ordering between half of the corner-shared octahedra; (B) antiferromagnetic (ferromagnetic) ordering along all corner (edge) shared octahedra. Figures 4(a) and 4(b) belong to the former and latter categories of kind (A). Here the two edge-shared sublattices are simply connected by an inversion combined with time reversal \mathcal{T} . As a result within the nonrelativistic limit the up and down spin channels are completely degenerate [see Figs. 4(d), 4(e)] throughout the whole BZ. Inclusion of SOC stabilizes a relative spin canting between the corner-shared sites for both Figs. 4(a) and 4(b) magnetic arrangements. There exist two stable compensated noncollinear magnetic arrangements originating from kind (A) belonging to the different magnetic space groups $P2_1/c'$ and $P2_1/c$ due to different spin quantization axes. The edge-shared spins are rotated spatially by 68.8° and 88.2° for $P2_1/c'$ and $P2_1/c$, respectively. Our theoretical calculation within the GGA + SOC+ U scheme suggests the latter to be 17.3 meV/u.c. higher in energy than the AFM ground state $P2_1/c'$. The magnetic space group symmetry of the ground state $P2_1/c'$ includes ϵ , PT , $\mathbf{t}_m C_{2y}$, and $\mathbf{t}_m \mathcal{T}\mathcal{M}_y$, where translation vector \mathbf{t}_m is $(0, \frac{1}{2}, \frac{1}{2})$. The SOC lifts the fourfold degeneracy of the bands, but the Kramers degeneracy remain intact even in the presence of SOC due to its PT symmetry. We have plotted the spin configuration in Fig. 4(c) and the corresponding band dispersion [in Fig. 4(f)] for the higher-energy state of kind (B). Here the Re sites with opposite spins are only connected through $\mathcal{T}\{C_4t\}$, which offers a possibility of altermagnetic-pair bands from symmetry consideration. The splitting between altermagnetic pairs is relatively small (~ 0.3 eV) which is of the order of SOC-induced band splitting of the system [see yellow line in Fig. 4(f)]. The AM $P2_1/c$ configuration and FM state are 28.6 meV and 185.9 meV higher than the AFM ground state of the monoclinic

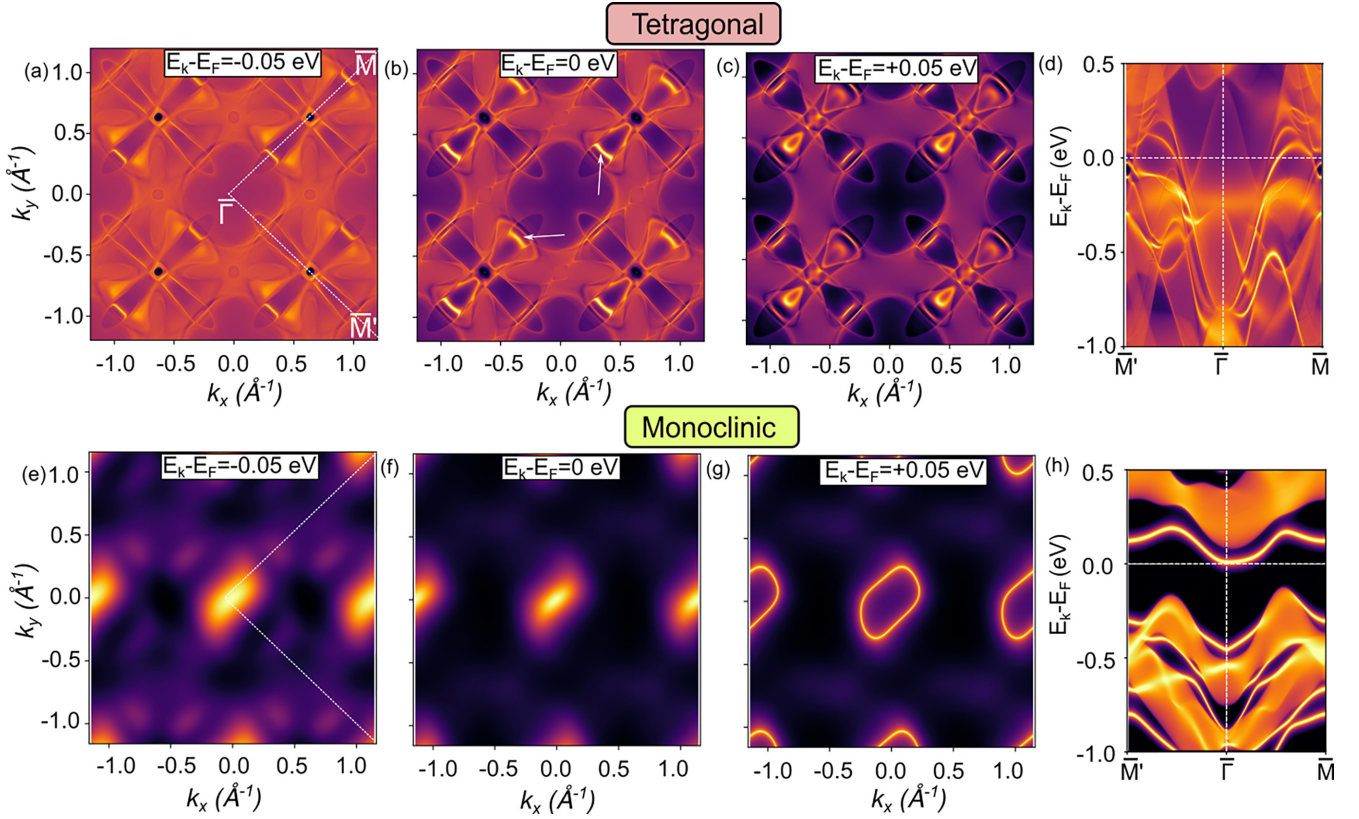


FIG. 5. Spectral function and surface state topology. The surface state arc near the Fermi energy for both tetragonal R - ReO_2 (a)–(c) and monoclinic α - ReO_2 (e)–(g) phases. The spectral functions over two orthogonal $\Gamma\bar{M}$ momentum paths are shown as a function of energy in (d) and (h) for tetragonal and monoclinic phases, respectively. The open surface Fermi arcs along the $\Gamma\bar{M}$ directions of R - ReO_2 are shown with white arrows. (a) and (c) show the arc structure at E_F . (b) is robust against small change in the energy that may originate from finite surface potentials. We observe closed-loop surface spectral function slightly below the Fermi energy, at $E = E_F + 0.05$ eV for monoclinic phase as shown in (f). The surface state becomes detached with increasing energy value as seen in (h).

phase. Among all these possible magnetic orders, AFM spin configuration commensurate with magnetic space group $P2_1/c'$ has the lowest energy. Contrary to metallic AM state of the tetragonal phase, the ground state of monoclinic α - ReO_2 is insulating with a band gap value of ~ 0.19 eV. Along with strain-induced AFM to AM transition from α - and R - ReO_2 , it also undergoes MIT which is a useful experimental signature to track the phase transition.

D. Contrasting surface states between AM and AFM phases

Conventionally R - and α - ReO_2 belong to two different elementary classes of magnetism. The PT is preserved for the AFM ground state of α - ReO_2 , whereas the opposite sublattices in R - ReO_2 are connected by the $C_{4z}\mathcal{T}$ symmetry. As a result we find strong momentum-dependent altermagnetic-pair splitting of ~ 1 eV in R - ReO_2 while the Kramers degeneracy is present for the monoclinic ground state. These dissimilarities in magnetic nature percolate to the sharply contrasting surface properties of these phases, which can be observed by, e.g., angle-resolved photoemission spectroscopy (ARPES). The surface spectral function can be obtained from the following relation of the retarded Green's function (G_r)

[33] in the 2D momentum \mathbf{k}_{\parallel} at frequency ω :

$$A(\mathbf{k}_{\parallel}, \omega) = -\frac{1}{\pi} \lim_{\eta \rightarrow 0^+} \text{Im} \text{Tr}[G_s(\mathbf{k}_{\parallel}, \omega + i\eta)]. \quad (6)$$

Figure 5 includes the constant energy contours calculated by creating a finite slab geometry along the (001) direction with magnetic anisotropy along the z axis. The arc of spectral functions of R - [α -] ReO_2 is plotted for $E - E_F = -0.05$ eV, 0 eV, and $+0.05$ eV in panels (a) [(e)], (b) [(f)], and (c) [(g)], respectively. There exists a pair of open Fermi surface arcs along the $\bar{\Gamma}\bar{M}$ direction. Given the surface sensitivity and probing depth of the experimental technique, there exists a finite uncertainty of the Fermi energy. We find that these paired surface arcs are robust with small variation of energy around E_F that can be induced by surface potentials. In Fig. 5(f) we see the Fermi arc forms a closed-loop structure around the $\bar{\Gamma}$ point near E_F for the monoclinic phase. The surface loop resides well within the bulk gap without connecting the conduction and valence sectors which makes it trivial in nature. The distorted surface loop shows the asymmetric nature along two orthogonal directions of the BZ. With decreasing binding energy, the surface arc detaches from the Fermi energy as can be seen in Figs. 5(e) and 5(f).

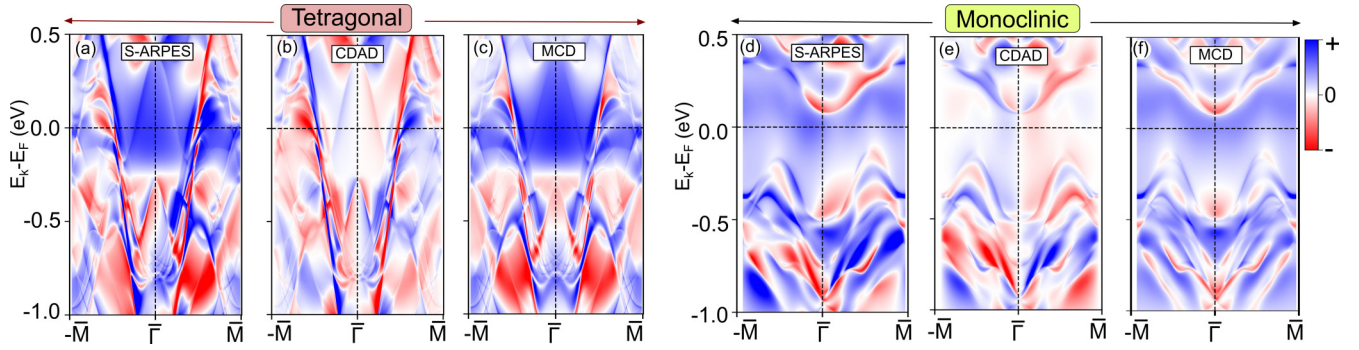


FIG. 6. Spin-ARPES calculations. Spin-polarized surface spectral function, $S(\mathbf{k}_{\parallel}, \omega)$, for both R - ReO_2 (a) and α - ReO_2 (d) along two opposite momentum paths. The antisymmetric part, CDAD (symmetric part, MCD) of the S-ARPES for opposite momentum transfer is plotted in panel (b) (panel (c)) and panel (e) (panel (f)) for R - ReO_2 and α - ReO_2 phases, respectively. The MCD spectra of tetragonal phase is primarily contributed from the bulk states conveying the internal TRS breaking of the AM R - ReO_2 . Both of the CDAD and MCD in α - ReO_2 originate the broken P and \mathcal{T} symmetry, combined with SOC.

In Figs. 5(d) and 5(h) the spectral functions contributed from both bulk and surface states are plotted as a function of energy along orthogonal $\bar{M}\bar{\Gamma}\bar{M}$ paths [white dashed line in Fig. 5(a)] for tetragonal and monoclinic phases, respectively. We see an isolated surface state within the bulk gap just above the Fermi energy of α - ReO_2 . The asymmetry of the surface state between two orthogonal paths verifies the distorted surface loop structure of Fig. 5(g).

E. Spin-polarized spectral functions

There exist unique spin textures in the momentum-resolved surface spectral function of altermagnetic and antiferromagnetic materials as a consequence of the nontrivial ground state magnetism. In this section we compare the spin-polarized ARPES spectra between the two phases. The spin-polarized spectral functions [$S(\mathbf{k}_{\parallel}, \omega)$] can be calculated from the following expression:

$$S(\mathbf{k}_{\parallel}, \omega) = -\frac{1}{\pi} \lim_{\eta \rightarrow 0^+} \text{Im Tr}[\boldsymbol{\sigma} G_s(\mathbf{k}_{\parallel}, \omega + i\eta)]/A(\mathbf{k}_{\parallel}, \omega). \quad (7)$$

Here the $\boldsymbol{\sigma}$'s are the Pauli matrices. We have plotted the spin-polarized spectral functions along two opposite momentum $\bar{\Gamma}\bar{M}$ paths for both R - and α - ReO_2 in Fig. 6. The pronounced asymmetric nature of S-ARPES confirms the presence of both symmetric and antisymmetric parts with respect to the opposite momentum direction. First we consider the spectral function plots of the tetragonal phase as shown in Figs. 6(a)–6(c). We calculate circular dichroism in the angular distribution (CDAD), arising from the experimental geometry. CDAD is primarily antisymmetric for opposite momentum due to broken inversion symmetry at the surface. Apart from the CDAD, there exists an additional symmetric part of the spin-polarized ARPES (S-ARPES), namely magnetic circular dichroism (MCD), which indicates the spin polarization of the system and is directly connected to TRS breaking in momentum space. Comparison of Figs. 6(b) and 6(c) with the spin-integrated spectral function along the $\bar{\Gamma}\bar{M}$ path [see in Fig. 5(d)] suggests the CDAD is pronounced in the surface-state-dominated momentum points. Contrarily the MCD arises primarily from bulk spectral regions

for R - ReO_2 . The significantly larger magnitude of the MCD spectra contributed from bulk states substantiate the intrinsic TRS breaking within the bulk beyond any surface-dominated affects, whereas the CDAD counterpart comes primarily from surface geometry, near the Fermi energy. Recent experimental studies report symmetric MCD spectra as an identification of the TRS-breaking spin splitting in the sister altermagnetic tetragonal compound RuO_2 [34,52,53].

Next we analyze the α - ReO_2 S-ARPES plots for the (001) surface convoluted with the bulk in Figs. 6(d)–6(f). Unlike the tetragonal phase, both CDAD and MCD have comparable intensity. The absence of individual P and \mathcal{T} symmetry within the ground state AFM configuration coupled with surface-mediated contributions [54,55] leads to asymmetry between the states with $E_{\mathbf{k}}$ and $E_{-\mathbf{k}}$, which essentially gives rise to different spin-ARPES spectra for opposite momentum [56]. This asymmetry within the spin-polarized spectral function of the ground state AFM leads to a small MCD contribution at the α - ReO_2 . The calculation of these spectral features as a function of strain demonstrates in particular how they arise from different physical origin.

IV. CONCLUSION

In summary, we have presented strain-induced structural and magnetic transition accompanied with MIT between the conventional PT -symmetric AFM to AM phase for exploring technical applications. The bulk monoclinic α - ReO_2 phase is compensated AFM in nature with finite spin canting between two neighboring corner-shared octahedral Re sites. The ground state of the monoclinic phase is an insulator and accommodates the Kramers degenerate doublets, even in the presence of SOC, whereas the high-pressure R - ReO_2 phase hosts unique altermagnetism with d -wave spin order. The distinct magnetic order between the two phases is reflected in the contrasting surface state spectra. The pronounced MCD spectra obtained from our spin-polarized spectral function calculations confirms the intrinsic exchange-driven TRS-broken state in R - ReO_2 , which serves as an experimental verification of the AM state. Our study provides evidence of strain-tuning the conventional AFM state to the new third-category AM magnets.

ACKNOWLEDGMENTS

A.C. acknowledges financial support from an Alexander von Humboldt postdoctoral fellowship. We acknowledge funding by the Deutsche Forschungsgemeinschaft (DFG, German Research Foundation) TRR288-422213477 (Project No. A09). L.S. acknowledges support by the Grant Agency of the Czech Republic, Grant No. 19-28375X. We acknowledge the high-performance computational facility of supercomputer ‘‘Mogon’’ at Johannes Gutenberg Universitat Mainz, Germany. We acknowledge Roser Valenti and Rodrigo Jaeschke-Ubiergo for stimulating discussions.

APPENDIX A: GROUP-THEORETICAL DESCRIPTION OF *d*-WAVE ALTERMAGNET

To explain the spin texture and energetics of AMs we need to go beyond the usual magnetic group and consider spin group symmetry relations. In the usual magnetic space group the identical symmetry operations act simultaneously on both spin and real space, whereas any operations of a spin space group can be expressed as $[g_s||S_r]$, where g_s is any point symmetry operation acting only on the spin space and S_r represents real-space crystal symmetry which includes point symmetry g_r in combination with translation t . The spin groups can be expressed as a direct product of $\mathbf{r}_s \times \mathbf{R}_s$, where \mathbf{r}_s and \mathbf{R}_s are respectively spin-only groups and nontrivial spin groups. The generic form of \mathbf{R}_s for AM systems within the spin Laue group can be expressed as [2,3]

$$\mathbf{R}_s = [E||\mathbf{H}] + [C_2||\mathbf{G} - \mathbf{H}]. \quad (\text{A1})$$

Here \mathbf{H} is the halving subgroup of a crystallographic Laue group \mathbf{G} . For tetragonal $R\text{-ReO}_2$, $4/mmm$ is the point group \mathbf{G} corresponding to its crystallographic space group $P4_2/mmm$ and halving group $\mathbf{H} = mmm$. The fourfold crystal rotation C_{4z} within \mathbf{H} combines with C_2 rotation which changes the spin orientation between the different sublattices. The symmetry relations promote the fourfold alternating spin texture as can be seen in Fig. 2 of the main text consistent with the *d*-wave nature of the AM order parameter.

Here we list the symmetry operations of space group $P4_2/mmm$ used in the main text:

ϵ : the identity;

P : the inversion;

C_{2i} : a rotation of π around the \hat{i} axis, where $\hat{i} = \hat{x}, \hat{y}, \hat{z}$;

$C_{2d(2d\perp)}$: a rotation of π around the $\hat{x} + \hat{y}$ ($\hat{x} - \hat{y}$) axis;

\mathcal{M}_i : a mirror operation with respect to the j - k plane, where i, j, k are one of the x, y, z axes;

$\mathcal{M}_{d(d\perp)}$: a mirror operation with respect to the plane having normal along $\hat{x} + \hat{y}$ ($\hat{x} - \hat{y}$) axis.

APPENDIX B: EFFECT OF CORRELATION ON ALTERMAGNETIC STATE

Our first-principles electronic structure calculations suggest that the metallic AM ground state of $R\text{-ReO}_2$ is robust with respect to Coulomb correlations. We have plotted the nonrelativistic energy dispersion of the AM state of $R\text{-ReO}_2$

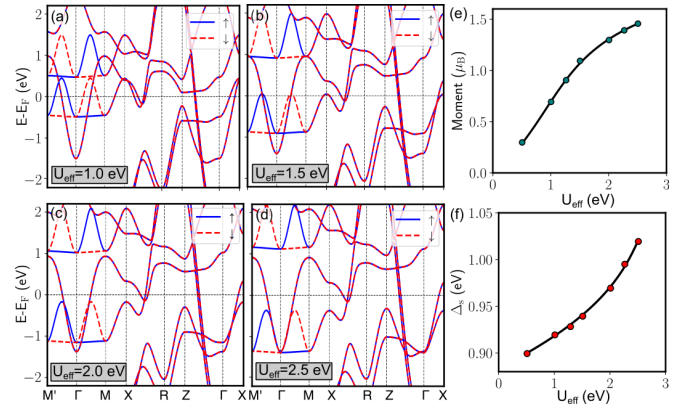


FIG. 7. Band structure of AM $R\text{-ReO}_2$ within GGA+ U scheme in absence of SOC for Hubbard $U_{\text{eff}} = 1.0$ eV (a), $U_{\text{eff}} = 1.5$ eV (b), $U_{\text{eff}} = 2.0$ eV (c), and $U_{\text{eff}} = 2.5$ eV (d). Here $U_{\text{eff}} = U - J_H$. Variation of spin moment per Re atom and maximum spin splitting near the Fermi energy with respect to effective Hubbard U are plotted in (e) and (f), respectively.

for a range of Hubbard U values in Figs. 7(a)–7(d). We expect the effect of Coulomb correlation for this compound as the magnetic building block Re is a $5d$ element. The magnetic moment/Re atoms and nonrelativistic spin splitting near the Fermi energy are plotted as a function of Hubbard U in Figs. 7(e) and 7(f), respectively. Increase in U enhances the localization of the Re- d orbital further at the atomic cite hence increases the magnetic moment/Re. The altermagnetic spin splitting Δ_s increases slowly with increase of Hubbard U value.

APPENDIX C: IMPACT OF DOPING ON GROUND STATE ANISOTROPY

Here we highlight that introduction of electron or hole doping [see Fig. 8(a)] can necessitate a characteristic change in the system by altering the magnetization direction. In Fig. 8 we have plotted the magnetocrystalline anisotropy, $E_{[100]} - E_{[001]}$ (a) and change in Fermi energy (b) as a function of electron occupancy, n_e . The equilibrium electron count of the system is marked with yellow star. We see for finite electron doping the easy-plane spin anisotropy has lower energy than the out-of-plane spin configurations. Our calculation

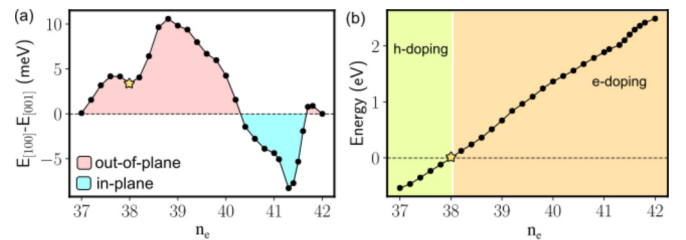


FIG. 8. (a) Magnetocrystalline anisotropy energy, $E_{[100]} - E_{[001]}$, as a function of electron occupancy (n_e). Finite electron doping opens the possibility to tune Neel vector along in-plane direction. (b) Fermi energy of the ground state for different electron occupancy. The electron (e) and hole (h) doped regimes are marked in orange and green colors, respectively.

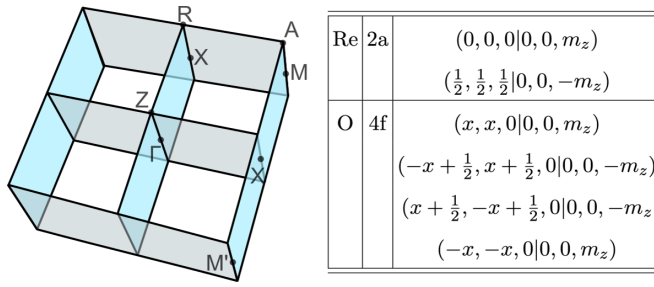


FIG. 9. Left: The BZ of $R\text{-ReO}_2$ with high-symmetry k points marked on it. The nonrelativistic spin-degenerate nodal surfaces of the AP bands are shown with colored planes. Right: The magnetic Wyckoff positions of $R\text{-ReO}_2$ in ground state magnetic space group $P4'_2'/mmm'$.

illustrates the potential to adjust the orientation of the easy axis through off-stoichiometry or alloying.

APPENDIX D: SYMMETRY ANALYSIS AND NODAL PLANE

The tetragonal $R\text{-ReO}_2$ is AM in nature as has been discussed in the main text. In Fig. 9 we have plotted the nodal surfaces between the AP of $R\text{-ReO}_2$ within the nonrelativistic limit. The transposing mirror symmetries $[C_2||\mathcal{M}_x]$ and $[C_2||\mathcal{M}_y]$ protect these nodal surfaces which are commensurate with the d -wave AM nature. Inclusion of SOC lifts up the degeneracy of altermagnetic-pair bands in different momentum points and promotes unique nodal crossings. The nature and shape of the nodal line crucially depends on the choice of spin quantization axis as described in the main text.

The Wyckoff positions and corresponding allowed magnetic moment configurations are listed in Fig. 9 for the ground state $P4'_2'/mmm'$. The allowed moment direction of the ground state confirms that $R\text{-ReO}_2$ prefers collinear magnetic configuration even in presence of spin-orbit coupling due to crystal symmetry.

- [1] L. Šmejkal, R. González-Hernández, T. Jungwirth, and J. Sinova, Crystal time-reversal symmetry breaking and spontaneous Hall effect in collinear antiferromagnets, *Sci. Adv.* **6**, eaaz8809 (2020).
- [2] L. Šmejkal, J. Sinova, and T. Jungwirth, Beyond conventional ferromagnetism and antiferromagnetism: A phase with nonrelativistic spin and crystal rotation symmetry, *Phys. Rev. X* **12**, 031042 (2022).
- [3] L. Šmejkal, J. Sinova, and T. Jungwirth, Emerging research landscape of altermagnetism, *Phys. Rev. X* **12**, 040501 (2022).
- [4] I. I. Mazin, K. Koepf, M. D. Johannes, R. González-Hernández, and L. Šmejkal, Prediction of unconventional magnetism in doped FeSb_2 , *Proc. Natl. Acad. Sci. USA* **118**, e2108924118 (2021).
- [5] I. Mazin, Editorial: Altermagnetism—a new punch line of fundamental magnetism, *Phys. Rev. X* **12**, 040002 (2022).
- [6] L. Šmejkal, A. B. Hellènes, R. González-Hernández, J. Sinova, and T. Jungwirth, Giant and tunneling magnetoresistance in unconventional collinear antiferromagnets with nonrelativistic spin-momentum coupling, *Phys. Rev. X* **12**, 011028 (2022).
- [7] R. Jaeschke-Ubiergo, V. K. Bharadwaj, T. Jungwirth, L. Šmejkal, and J. Sinova, Supercell altermagnets, *Phys. Rev. B* **109**, 094425 (2024).
- [8] X. Zhou, W. Feng, R.-W. Zhang, L. Šmejkal, J. Sinova, Y. Mokrousov, and Y. Yao, Crystal thermal transport in altermagnetic RuO_2 , *Phys. Rev. Lett.* **132**, 056701 (2024).
- [9] S. Reimers, L. Odenbreit, L. Šmejkal, V. N. Strocov, P. Constantinou, A. B. Hellènes, R. J. Ubiergo, W. H. Campos, V. K. Bharadwaj, A. Chakraborty, T. Denneulin, W. Shi, R. E. Dunin-Borkowski, S. Das, M. Kläui, J. Sinova, and M. Jourdan, Direct observation of altermagnetic band splitting in CrSb thin films, *Nat. Commun.* **15**, 2116 (2024).
- [10] D. Litvin and W. Opechowski, Spin groups, *Physica* **76**, 538 (1974).
- [11] D.-F. Shao, S.-H. Zhang, M. Li, C.-B. Eom, and E. Y. Tsymbal, Spin-neutral currents for spintronics, *Nat. Commun.* **12**, 7061 (2021).
- [12] R. González-Hernández, L. Šmejkal, K. Výborný, Y. Yahagi, J. Sinova, T. Jungwirth, and J. Železný, Efficient electrical spin splitter based on nonrelativistic collinear antiferromagnetism, *Phys. Rev. Lett.* **126**, 127701 (2021).
- [13] A. Bose, N. J. Schreiber, R. Jain, D.-f. Shao, H. P. Nair, J. Sun, X. S. Zhang, D. A. Muller, E. Y. Tsymbal, D. G. Schlom, and D. C. Ralph, Tilted spin current generated by the collinear antiferromagnet ruthenium dioxide, *Nat. Electron.* **5**, 267 (2022).
- [14] H. Bai, L. Han, X. Y. Feng, Y. J. Zhou, R. X. Su, Q. Wang, L. Y. Liao, W. X. Zhu, X. Z. Chen, F. Pan, X. L. Fan, and C. Song, Observation of spin splitting torque in a collinear antiferromagnet RuO_2 , *Phys. Rev. Lett.* **128**, 197202 (2022).
- [15] S. Karube, T. Tanaka, D. Sugawara, N. Kadoguchi, M. Kohda, and J. Nitta, Observation of spin-splitter torque in collinear antiferromagnetic RuO_2 , *Phys. Rev. Lett.* **129**, 137201 (2022).
- [16] Z. Feng, X. Zhou, L. Šmejkal, L. Wu, Z. Zhu, H. Guo, R. González-Hernández, X. Wang, H. Yan, P. Qin, X. Zhang, H. Wu, H. Chen, Z. Meng, L. Liu, Z. Xia, J. Sinova, T. Jungwirth, and Z. Liu, An anomalous Hall effect in altermagnetic ruthenium dioxide, *Nat. Electron.* **5**, 735 (2022).
- [17] R. D. Gonzalez Betancourt, J. Zubáč, R. Gonzalez-Hernandez, K. Geishendorf, Z. Šobán, G. Springholz, K. Olejník, L. Šmejkal, J. Sinova, T. Jungwirth, S. T. B. Goennenwein, A. Thomas, H. Reichlová, J. Železný, and D. Kriegner, Spontaneous anomalous Hall effect arising from an unconventional compensated magnetic phase in a semiconductor, *Phys. Rev. Lett.* **130**, 036702 (2023).
- [18] Y. Guo, H. Liu, O. Janson, I. C. Fulga, J. van den Brink, and J. I. Facio, Spin-split collinear antiferromagnets: A large-scale ab-initio study, *Mater. Today Phys.* **32**, 100991 (2023).
- [19] J. A. Ouassou, A. Brataas, and J. Linder, dc Josephson effect in altermagnets, *Phys. Rev. Lett.* **131**, 076003 (2023).
- [20] J.-H. Chu, J. G. Analytis, K. De Greve, P. L. McMahon, Z. Islam, Y. Yamamoto, and I. R. Fisher, In-plane resistivity anisotropy in an underdoped iron arsenide superconductor, *Science* **329**, 824 (2010).
- [21] C. W. Hicks, D. O. Brodsky, E. A. Yelland, A. S. Gibbs, J. A. N. Bruin, M. E. Barber, S. D. Edkins, K. Nishimura, S.

- Yonezawa, Y. Maeno, and A. P. Mackenzie, Strong increase of T_c of Sr_2RuO_4 under both tensile and compressive strain, *Science* **344**, 283 (2014).
- [22] J. Mutch, W.-C. Chen, P. Went, T. Qian, I. Z. Wilson, A. Andreev, C.-C. Chen, and J.-H. Chu, Evidence for a strain-tuned topological phase transition in ZrTe_5 , *Sci. Adv.* **5**, eaav9771 (2019).
- [23] Z. Xu, M. Ye, J. Li, W. Duan, and Y. Xu, Hydrostatic pressure-induced magnetic and topological phase transitions in the MnBi_2Te_4 family of materials, *Phys. Rev. B* **105**, 085129 (2022).
- [24] L. Li, G. Hu, Y. Qi, and I. Umehara, Hydrostatic pressure effect on magnetic phase transition and magnetocaloric effect of metamagnetic TmZn compound, *Sci. Rep.* **7**, 42908 (2017).
- [25] S.-S. Wang, Y. Liu, Z.-M. Yu, X.-L. Sheng, and S. A. Yang, Hourglass Dirac chain metal in rhenium dioxide, *Nat. Commun.* **8**, 1844 (2017).
- [26] D. Hirai, T. Anbai, S. Uji, T. Oguchi, and Z. Hiroi, Extremely large magnetoresistance in the hourglass Dirac loop chain metal $\beta\text{-ReO}_2$, *J. Phys. Soc. Jpn.* **90**, 094708 (2021).
- [27] S. Shibata, Y. Hirose, A. Chikamatsu, E. Ikenaga, and T. Hasegawa, Strain-induced structural transition of rutile type ReO_2 epitaxial thin films, *Appl. Phys. Lett.* **117**, 111903 (2020).
- [28] A. Ivanovskii, T. Chupakhina, V. Zubkov, A. Tyutyunnik, V. Krasilnikov, G. Bazuev, S. Okatov, and A. Lichtenstein, Structure and electronic properties of new rutile-like rhenium (IV) dioxide ReO_2 , *Phys. Lett. A* **348**, 66 (2005).
- [29] Y. L. Li and Z. Zheng, Structural, elastic and electronic properties of ReO_2 , *Chin. Phys. Lett.* **25**, 4086 (2008).
- [30] J. Bailey, The monoclinic-tetragonal transformation and associated twinning in thin films of zirconia, *Proc. R. Soc. London A* **279**, 395 (1964).
- [31] D. Simeone, G. Baldinozzi, D. Gosset, M. Dutheil, A. Bulou, and T. Hansen, Monoclinic to tetragonal semireconstructive phase transition of zirconia, *Phys. Rev. B* **67**, 064111 (2003).
- [32] E. B. Asgerov, A. I. Beskrovnyy, N. V. Doroshkevich, C. Mita, D. M. Mardare, D. Chicea, M. D. Lazar, A. A. Tatarinova, S. I. Lyubchyk, S. B. Lyubchyk, A. I. Lyubchyk, and A. S. Doroshkevich, Reversible martensitic phase transition in yttrium-stabilized ZrO_2 nanopowders by adsorption of water, *Nanomaterials* **12**, 435 (2022).
- [33] A. Damascelli, Probing the electronic structure of complex systems by ARPES, *Phys. Scr.* **T109**, 61 (2004).
- [34] O. Fedchenko, J. Minar, A. Akashdeep, S. W. D'Souza, D. Vasilyev, O. Tkach, L. Odenbreit, Q. L. Nguyen, D. Kutnyakhov, N. Wind, L. Wenthous, M. Scholz, K. Rossnagel, M. Hoesch, M. Aeschlimann, B. Stadtmueller, M. Klauui, G. Schoenhense, G. Jakob, T. Jungwirth *et al.*, Observation of time-reversal symmetry breaking in the band structure of altermagnetic RuO_2 , *Sci. Adv.* **10**, eadj4883 (2024).
- [35] J. P. Perdew, K. Burke, and M. Ernzerhof, Generalized gradient approximation made simple, *Phys. Rev. Lett.* **77**, 3865 (1996).
- [36] P. E. Blöchl, Projector augmented-wave method, *Phys. Rev. B* **50**, 17953 (1994).
- [37] G. Kresse and D. Joubert, From ultrasoft pseudopotentials to the projector augmented-wave method, *Phys. Rev. B* **59**, 1758 (1999).
- [38] G. Kresse and J. Hafner, *Ab initio* molecular dynamics for liquid metals, *Phys. Rev. B* **47**, 558 (1993).
- [39] G. Kresse and J. Furthmüller, Efficient iterative schemes for *ab initio* total-energy calculations using a plane-wave basis set, *Phys. Rev. B* **54**, 11169 (1996).
- [40] S. L. Dudarev, G. A. Botton, S. Y. Savrasov, C. J. Humphreys, and A. P. Sutton, Electron-energy-loss spectra and the structural stability of nickel oxide: An LSDA+U study, *Phys. Rev. B* **57**, 1505 (1998).
- [41] I. Souza, N. Marzari, and D. Vanderbilt, Maximally localized Wannier functions for entangled energy bands, *Phys. Rev. B* **65**, 035109 (2001).
- [42] Q. S. Wu, S. N. Zhang, H.-F. F. Song, M. Troyer, and A. A. Soluyanov, WannierTools: An open-source software package for novel topological materials, *Comput. Phys. Commun.* **224**, 405 (2018).
- [43] F. D. Murnaghan, The compressibility of media under extreme pressures, *Proc. Natl. Acad. Sci. USA* **30**, 244 (1944).
- [44] F. Birch, Finite elastic strain of cubic crystals, *Phys. Rev.* **71**, 809 (1947).
- [45] M. De Raychaudhury, T. Saha-Dasgupta, and D. D. Sarma, Theoretical study of doped $\text{Ti}_2\text{Mn}_2\text{O}_7$ and $\text{Ti}_2\text{Mn}_2\text{O}_7$ under pressure, *Phys. Rev. B* **75**, 014443 (2007).
- [46] A. S. Disa, M. Fechner, T. F. Nova, B. Liu, M. Först, D. Prabhakaran, P. G. Radaelli, and A. Cavalleri, Polarizing an antiferromagnet by optical engineering of the crystal field, *Nat. Phys.* **16**, 937 (2020).
- [47] R. Kumar, T. Dey, P. M. Ette, K. Ramesha, A. Chakraborty, I. Dasgupta, J. C. Orain, C. Baines, S. Tóth, A. Shahee, S. Kundu, M. Prinz-Zwick, A. A. Gippius, N. Büttgen, P. Gegenwart, and A. V. Mahajan, Unconventional magnetism in the $4d^4$ -based $S = 1$ honeycomb system $\text{Ag}_3\text{LiRu}_2\text{O}_6$, *Phys. Rev. B* **99**, 054417 (2019).
- [48] A. Chakraborty and I. Dasgupta, Study of electronic structure and magnetism in d^4 double perovskite iridates $A_2\text{ScIrO}_6$ ($A = \text{Ba}, \text{Sr}$), *J. Magn. Magn. Mater.* **492**, 165708 (2019).
- [49] A. Chakraborty, V. Kumar, S. Bachhar, N. Büttgen, K. Yokoyama, P. K. Biswas, V. Siruguri, S. Pujari, I. Dasgupta, and A. V. Mahajan, Unusual spin dynamics in the low-temperature magnetically ordered state of $\text{Ag}_3\text{LiIr}_2\text{O}_6$, *Phys. Rev. B* **104**, 115106 (2021).
- [50] S. Bhowal and I. Dasgupta, Spin-orbit effects in pentavalent iridates: Models and materials, *J. Phys.: Condens. Matter* **33**, 453001 (2021).
- [51] A. Bandyopadhyay, A. Chakraborty, S. Bhowal, V. Kumar, M. M. Sala, A. Efimenko, F. Bert, P. K. Biswas, C. Meneghini, N. Büttgen, I. Dasgupta, T. S. Dasgupta, A. V. Mahajan, and S. Ray, Breakdown of atomic spin-orbit coupling picture in an apparently isolated pseudo-one-dimensional iridate: $\text{Sr}_3\text{NaIrO}_6$, *Phys. Rev. B* **105**, 104431 (2022).
- [52] J. Krempaský, L. Šmejkal, S. W. D'Souza, M. Hajlaoui, G. Springholz, K. Uhlířová, F. Alarab, P. C. Constantinou, V. Stokov, D. Usanov, W. R. Pudelko, R. González-Hernández, A. B. Hellenes, Z. Jansa, H. Reichlová, Z. Šobáň, R. D. G. Betancourt, P. Wadley, J. Sinova, D. Krieger *et al.*, Altermagnetic lifting of Kramers spin degeneracy, *Nature (London)* **626**, 517 (2024).
- [53] S. Lee, S. Lee, S. Jung, J. Jung, D. Kim, Y. Lee, B. Seok, J. Kim, B. G. Park, L. Šmejkal, C.-J. Kang, and C. Kim, Broken Kramers degeneracy in altermagnetic MnTe , *Phys. Rev. Lett.* **132**, 036702 (2024).

- [54] O. V. Pylypovskiy, S. F. Weber, P. Makushko, I. Veremchuk, N. A. Spaldin, and D. Makarov, Surface-symmetry-driven Dzyaloshinskii-Moriya interaction and canted ferrimagnetism in collinear magnetoelectric antiferromagnet Cr_2O_3 , [arXiv:2310.13438](https://arxiv.org/abs/2310.13438).
- [55] A. Honma, D. Takane, S. Souma, Y. Wang, K. Nakayama, M. Kitamura, K. Horiba, H. Kumigashira, T. Takahashi, Y. Ando, and T. Sato, Unusual surface states associated with PT -symmetry breaking and antiferromagnetic band folding in NdSb , [Phys. Rev. B **108**, 115118 \(2023\)](https://doi.org/10.1103/PhysRevB.108.115118).
- [56] O. Fedchenko, L. Šmejkal, M. Kallmayer, Y. Lytvynenko, K. Medjanik, S. Babenkov, D. Vasilyev, M. Kläui, J. Demsar, G. Schönhense, M. Jourdan, J. Sinova, and H. J. Elmers, Direct observation of antiferromagnetic parity violation in the electronic structure of Mn_2Au , [J. Phys.: Condens. Matter **34**, 425501 \(2022\)](https://doi.org/10.1088/0953-4085/34/425501).